Journal of Applied Fluid Mechanics, Vol. 18 No. 1, pp. 2535-2549, 2025.
Available online at www.jafmonline.net, ISSN 1735-3572, EISSN 1735-3645.
https://doi.org/10.47176/jafm.18.10.3435

Investigation of the Effects of the Jet Impingement Angle on Torque Generation at the Suction Surface of a Pelton Turbine Bucket

Y. X. Liu [1,2,3†], Q. Zheng[1], L. H. Guo[4], X. Z. Wei[1,2,3], B. Xu[2,3], H. M. Wang[2,3], D. Q. Qin[2,3] and L. Han[5]

[1] College of Power and Energy Engineering, Harbin Engineering University, Harbin 150001, China
[2] Harbin Electric Machinery Co. Ltd., Harbin 150040, China
[3] Harbin Institute of Large Electrical Machinery Co. Ltd., Harbin 150040, China
[4] Datang Xizang Energy Development Co. Ltd., Lhasa 850001, China
[5] School of Energy Science and Engineering, Harbin Institute of Technology, Harbin 150001, China

†*Corresponding Author Email:* lyxin@hec-china.com

ABSTRACT

The performance of a Pelton turbine was investigated by means of an integrated numerical and experimental study that focused on the fluid dynamics associated with the bucket suction surface during the jet–bucket interactions. The transient pressure distributions and torque-generation mechanisms were characterized under a variety of conditions. The results revealed a distinct two-phase transition process: an initial high-pressure zone (θ = 48.7°) that generated a resistance torque was followed by a negative-pressure region (θ = 57.2°) that produced a significant torque enhancement. The impingement angle was quantitatively established as a primary control parameter since a direct correlation was observed between angle decreases and torque improvements. A thickness-based regulation method for the suction surface was developed to precisely control both the impingement angle and the subsequent jet trajectory. These results provide fundamental insights into the transient flow phenomena that affect the turbine efficiency and offer practical design guidelines for performance optimization in high-head hydropower applications. Critical knowledge gaps regarding the fluid mechanics of Pelton turbines were addressed using measurable benchmarks for bucket design improvements.

Article History

Received February 11, 2025
Revised April 11, 2025
Accepted May 11, 2025
Available online August 5, 2025

Keywords:

Hydropower
Pelton turbine bucket
Suction surface
Torque
Multiphase flow

1. INTRODUCTION

An adequate energy supply is essential for economic development because it is used to maintain industrial operations, transportation networks, and service industries. In addition, it is intrinsically linked to the pace of economic growth. Robust correlations have been observed between escalations in energy demands and expansions in national economies, and developing countries tend to exhibit these trends most markedly. For example, the rapid economic development that has occurred in China has precipitated a surge in energy consumption, which has catalyzed further investment and expansion in energy industries. In addition, the percentage of the total available energy in China that is accounted for by clean energy sources has substantially increased. As of 2023, the cumulative installed capacity of renewable energy sources in China surpassed 1.5 billion kW, which represents 51.9% of the total electricity generation capacity of the country. Solar and wind energy are the second and third largest contributors, respectively, to the national energy capacity (CREEI, 2023). Furthermore, nearly 40% of the global renewable-energy capacity is contributed by China.

The use of renewable energy sources can significantly mitigate greenhouse gas emissions (Zhao et al., 2025). Of the various types of renewable energy sources, hydroelectric power is one of the most established sources. It possesses significant operational flexibility, superior efficiency, and low maintenance requirements. Over the past 5 years, the average annual growth rate of new hydropower capacity has been 22 GW, which is less than the 45 GW that is needed annually to hold the global temperature increase below 1.5 °C and to reach net-zero emissions by 2050 (IHA, 2022). Because renewable energy sources are inherently variable and intermittent, they present supply-management challenges; however, since hydropower sources offer flexibility, they are crucial to the mitigation of these challenges. As Viollet (2017) emphasized, the proliferation of wind and solar energy sources has increased the operational demands on hydropower facilities by requiring them to adapt to fluctuating conditions. Unlike wind and solar energy sources, the output of hydropower sources can be rapidly modulated, thereby ensuring grid stability. Thus, hydropower sources serve as critical 'peak-shaving' resources because they effectively balance the electricity supply and demand. The 2020 directives from the Central Committee of the Communist Party of China regarding the drafting of the 14th Five-Year Plan for National Economic and Social Development and the long-term goals for 2035 emphasize the developmental potential of hydropower in the southwestern region of China (PRC, 2021). This area, which is defined by rugged terrain and significant river-flow variability, is optimally suited for the construction of high-head hydropower stations. By capitalizing on the natural advantages of this region, large-scale hydropower facilities can provide a stable power supply while facilitating the integration of wind and solar energies, thereby significantly aiding the advancement of China's dual carbon goals.

Pelton turbines excel in high-head conditions and are renowned for their adaptability and regulatory capabilities, thus being ideal for use in hydropower developments in the southwestern region of China. Pelton turbines would be particularly useful in challenging mountainous terrains where dam construction is fraught with complexities (Han et al., 2021, 2024). These turbines are ideally suited for high-head operations, as demonstrated by the Biedroun Hydropower Station, which functions with a head of approximately 1,869 m (Nedelcu et al., 2021). The operational principle that governs a Pelton turbine is based on momentum conservation (Solemslie & Dahlhaug, 2012), which enables the potential energy of stored water to be transformed into kinetic energy by means of a high-velocity jet. This kinetic energy is subsequently converted into mechanical energy due to interactions between the jet and the buckets of the turbine (Chitrakar et al., 2020). The efficacy of a Pelton turbine is fundamentally dependent upon the interactions between the jet and the buckets (Messa et al., 2019). An analysis performed by Perrig (2007) revealed that the flow within a Pelton turbine is transient, multiphase, and turbulent in nature; these characteristics pose significant challenges to fluid-dynamics modeling and cause traditional single-phase flow theories to be inapplicable. Consequently, designers are compelled to consider the complexities of gas–liquid two-phase flow as they refine the design parameters of Pelton turbines, thereby enhancing their hydraulic efficiencies. Many analytical and computational studies have been initiated around the world with the goal of improving upon conventional methods of optimizing the bucket geometry and furnishing insights into the optimization of Pelton turbines (Erazo et al., 2022). These efforts have resulted in a design paradigm that is heavily reliant upon the acumen of engineering expertise and validation that is accomplished by model testing. Therefore, the pursuit of a design that ensures both efficacy and reliability requires substantial allocations of time and financial resources.

The bucket impingement angle, which is an important determinant of Pelton turbine efficiency, has been widely investigated because it has a substantial influence on the energy-conversion characteristics of the turbine. Janetzky et al. (1998) and Zoppé et al. (2006) focused on the static aspects of the turbine buckets, neglecting the effects of the centrifugal and Coriolis forces, as well as the free surface tension. They explored the impacts of incidence-angle variations on the pressure and torque dynamics. A comprehensive numerical and experimental study conducted by Perrig et al. (2006) revealed that the impingement angle critically affects the pressure-field characteristics and torque-generation patterns in distinct bucket regions. A quantitative analysis determined that the direct impingement zone is the primary contributor to the overall energy-conversion efficiency. Padhy and Saini (2009) investigated the effects of the impingement angle on bucket erosion in a Pelton turbine. It was demonstrated that smaller impingement angles can mitigate erosion damage but they compromise the energy-conversion efficiency. Zhang (2017) developed an efficiency model for Pelton turbines that is based on the principles of momentum. This incorporates several variables, such as the velocity ratio, viscous friction, and the jet-escape phenomenon. The results demonstrate that a 90° jet-impingement angle produces the optimal energy-conversion efficiency. Computational fluid dynamics (CFD) simulations (Zhao et al., 2023a) also confirmed that the maximum energy-conversion efficiency is obtained at a jet–bucket impingement angle of 90° because this angle leads to ideal momentum transfer. Mirza et al. (2024) experimentally investigated the effects of three jet impingement angles (75, 90, and 105°) on the bucket performance under stationary conditions; they then used their results to elucidate the underlying mechanisms that govern the patterns and severity of angle-dependent erosion.

Pelton turbines are inherently susceptible to a variety of factors that can lead to energy losses, such as water splashing from the rear of the bucket, jet atomization, water-layer interference, and secondary flows within the jet (Zeng, et al., 2016; Suyesh et al., 2019). However, while the studies discussed above provide an important theoretical and experimental foundation, they primarily focused on the angle of impingement on the pressure surface. There is a significant knowledge gap regarding turbine operation under variable suction-surface conditions, as well as insufficient quantitative analysis of the effects of changes in single variables on the impingement angle. This study was conducted to accomplish two primary goals: (1) to investigate the influence of the suction surface on the pressure within the bucket; and (2) to demonstrate how dynamic changes in the relative position of the suction surface affect the torque. The second was to establish a relationship between the geometric dimensions of the cutting edge of the bucket and the jet parameters, thereby providing insight into how different jet impingement angles affect the turbine performance.

2. MATHEMATICAL MODEL AND METHODS

2.1 Multiphase Flow Models

An examination of the hydraulic efficiencies of turbines revealed that Pelton turbines exhibit dynamic traits that are markedly different from those of reaction turbines. The fluctuating nature of both the temporal and spatial characteristics of the water flow within the rotating buckets of a Pelton turbine leads to a variable hydraulic efficiency (Xiao et al., 2007). In this context, the water and air are both incompressible and viscous fluids, and it is assumed that no heat is transferred as the water flows through the turbine. Therefore, the use of a two-phase flow model is crucial to the precise modeling of the free surface flow, which is an unsteady, three-dimensional, viscous, and incompressible flow (Jošt et al., 2010). To accurately depict the gas–liquid boundary, the volume of fluid technique and a homogeneous multiphase model were adopted during this study. This method can be used to monitor the phase interface because it resolves the momentum equations using an approach that considers both the density and the viscosity. In this framework, various parameters, such as the velocity, the turbulent kinetic energy, and the pressure, remain consistent across different phases; this consistency enables the generation of numerical results that closely match the experimental data while maintaining manageable computational expenses.

During this investigation, the ANSYS CFX software was used as the simulation tool. This software is a platform that is renowned for its advanced analytical capabilities when used for rotating machinery. It is widely acknowledged to be the industry standard for CFD simulations in these contexts. A thorough investigation of the equations that govern the multiphase flow, as presented in Eq. (1), was conducted during this study (Zeng, 2018):

$$\begin{cases} \frac{\partial \rho}{\partial t} + \frac{\partial \rho u_i}{\partial x_i} = 0 \\ \frac{\partial \rho u_i}{\partial t} + \frac{\partial \rho u_i u_j}{\partial x_i} = -\frac{\partial \rho_i}{\partial x_i} + \frac{\partial \left(\tau_{ij} - \rho \overline{u_i u_j}\right)}{\partial x_i} + S_M \\ \frac{\partial a_w}{\partial t} + u_i \frac{\partial a_w}{\partial x_i} = 0 \end{cases} \tag{1}$$

In Eq. (1), a_a represents the volume fraction of air and a_w represents the volume fraction of water; together, these variables satisfy the relationship $a_a + a_w = 1$. In addition, ρ represents the air–water mixture density and can be expressed by $\rho = a_w \rho_w + a_a \rho_a$, τ is the stress tensor, which includes both normal and tangential components, S_M signifies the volume force, and $\rho u_i u_j$ denotes the Reynolds stress.

2.2 Turbulence Model and Governing Equation

In recent years, the SST k–ω model has been used in numerous research studies (Shahram et al., 2014). This model is an extension of the standard k–ω approach and incorporates the transport of turbulent shear stress. By adding shear-stress transport terms, it enhances the prediction accuracy of flows near wall boundaries while effectively accommodating the characteristics of free shear flows further from the walls. The SST k–ω model has been proven to produce results that are precise and reliable when used to simulate rotational shear flows with high Reynolds numbers (Smirnov et al., 2008, 2009). Therefore, it is particularly well-suited for analyses of the intricate flow patterns within Pelton turbines (Fan et al., 2024).

The turbulent kinetic energy, k, and the specific dissipation rate, w', are two critical parameters of the transport equations in turbulence models. These parameters were thoroughly discussed by Menter in his 1994 study (Menter, 1994). The transport equations are provided next.

The kinematic eddy viscosity can be expressed by Eq. (2):

$$v_t = \frac{a_1 k}{max(a_1 w', SF_2)} \tag{2}$$

The turbulent kinetic energy can be represented by Eq. (3):

$$\frac{\partial \boldsymbol{k}}{\partial t} + U_j \frac{\partial k}{\partial x_j} = P_k - \beta^* k w' + \frac{\partial}{\partial x_j}\left[\left(v + \sigma_k v_t\right) \frac{\partial k}{\partial x_j}\right] \tag{3}$$

The specific dissipation rate is expressed by Eq. (4):

$$\frac{\partial w'}{\partial t} + U_j \frac{\partial w'}{\partial x_j} = aS^2 - \beta w'^2 + \frac{\partial}{\partial x_j}\left[\left(v + \sigma_{w'} v_t\right) \frac{\partial w'}{\partial x_j}\right] + 2(1 - F_1)\sigma_{w'^2} \frac{1}{w'} \frac{\partial k}{\partial x_i} \frac{\partial w'}{\partial x_i} \tag{4}$$

The closure coefficients and auxiliary relations are presented in Eq. (5):

$$\begin{cases} F_2 = tanh\left[\left[\frac{2\sqrt{k}}{\beta^* w' y}, \frac{500v}{y^2 w'}\right]^2\right] \\ P_k = min\left(\tau_{ij} \frac{\partial U_i}{\partial x_j}, 10\beta^* k w'\right) \\ F_1 = tanh\left\{\left\{min\left[max\left(\frac{\sqrt{k}}{\beta^* w' y}, \frac{500v}{y^2 w'}\right), \frac{4\sigma_{w'^2} k}{CD_{kw'} y^2}\right]\right\}^4\right\} \\ CD_{kw'} = max\left(2\rho\sigma_{w'^2} \frac{1}{w'} \frac{\partial k}{\partial x_i} \frac{\partial w'}{\partial x_i}, 10^{-10}\right) \end{cases} \tag{5}$$

In Eqs. (2)–(5), $a_1 = 5/9, a_2 = 0.44, \beta_1 = 3/40, \beta_2 = 0.0828, \beta^* = 9/100, \sigma_{k1} = 0.85, \sigma_{k2} = 1$, $\sigma_{w'1} = 0.5$, and $\sigma_{w'^2} = 0.856$. In addition, S represents the vorticity and y denotes the distance to the wall.

3. VERIFICATION AND VALIDATION

3.1 Computational Domain and Boundary Conditions

During the optimization of the computational modeling process for a turbine bucket, the complexity of the geometrical structure of the bucket necessitated the adoption of strategies that focused on enhancing computational efficiency and minimizing resource expenditure. As illustrated in Fig. 1, a simplified 1/2 scale model, which was constructed and meshed by the authors, was used during this study. The primary focus of this investigation was the flow dynamics within the bucket; thus, the distribution ring pipe was strategically omitted from the computational domain. The computational model therefore encompassed the runner

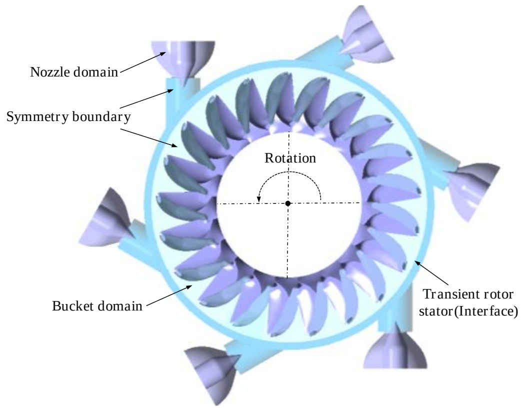

(a) Geometric characteristics of the computational domain

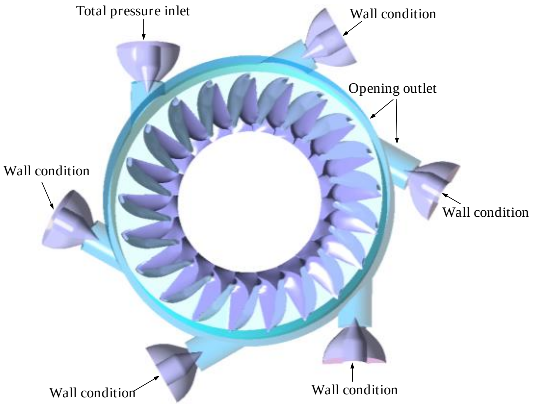

(b) Boundary conditions

Fig. 1 Schematic diagrams of the computational domain

and a portion of the nozzle pipe. Furthermore, since gravitational forces have negligible effects on the flow dynamics, it was determined that gravitational parameters were not required for this computational analysis.

After performing a comprehensive assessment of how various simulation tools perform for Pelton turbines, Židonis and Aggidis (2015) delivered an in-depth analysis and recommended the use of the ANSYS CFX software. The choice of the ANSYS CFX software is justified by its proven precision when used to model Pelton turbines. This precision is attributed to its advanced numerical algorithms and its ability to accurately simulate fluid dynamics phenomena, including free surface flow, turbulence, and the intricate interactions between gaseous and liquid phases. During the model-development stage of the study, the computational domain was discretized, after which the boundary conditions were defined. The torque generated by the interactions between the bucket and the jet was characterized by periodic variations. The focus of this study was the jet cutting process that occurred within the bucket. To optimize the computational efficiency and facilitate the analysis, only the torque variations induced by a single jet were considered.

For the simulations, a pressure inlet boundary was defined for a solitary nozzle, while the remaining nozzles were assigned wall boundary conditions. The wall boundary condition was used to represent physically inactive nozzles; it prevented backflow while maintaining geometric consistency. The pressure specified at the inlet of the straight nozzle was 586,236 Pa, which aligned with the experimental water head of 60 m.

At this inlet, the water volume fraction was set to 1, while the air volume fraction was 0; these volume fractions represent a pure-liquid inflow, which is typical of Pelton turbine operations. To simulate the interactions between the fluid and the solid surfaces, the channel walls were assigned no-slip boundary conditions. The standard wall functions, which are compatible with the selected SST k–ω turbulence model, were selected for the near-wall regions. At the interface that separated the moving and stationary domains, a transient rotor–stator model was implemented to account for the relative motion between these regions. The time step for the simulation was calculated according to the rated speed of the runner; it corresponded to a 0.5° rotation, thereby ensuring the dynamic fidelity of the simulation results by accurately capturing the state of the water flow inside the bucket. To solve the unsteady, two-phase, incompressible, turbulent flow equations, the finite volume method was used for spatial discretization. In addition, a coupled solver was adopted for the resolution of the governing equations. The coupled solver was selected because of its superior convergence capabilities when used in simulations of transient rotating machinery, for which the pressure–velocity coupling is strongly nonlinear. High-resolution schemes were used to discretize the momentum and pressure terms and thereby enhance the numerical precision. To ensure stability, the turbulence terms were discretized using a first-order scheme, which is recommended for SST k–ω simulations to prevent divergence. The transient scheme was discretized using a second-order backward Euler method; such discretization is crucial if the temporal accuracy is to be maintained and the overall stability of the computational process is to be enhanced.

3.2 Grid Generation and Grid Independence Verification

During this study, a tetrahedral meshing strategy was used for spatial discretization of both the runner and nozzle regions. To ensure uniformity in the mesh quality, each bucket domain was meticulously and separately discretized during the generation of the rotor mesh. This process involved definitions of the rotation center and periodic interfaces; these definitions facilitated the creation of a complete runner because they enabled rotational replication of the three-dimensional bucket. Given the complex surface contours and pronounced curvature variations within the bucket, mesh refinement was strategically applied in regions that were characterized by significant curvature, as illustrated in Fig. 2; these regions included the water-splitting edge, the cutting edge, and the forefield of the bucket. Particular focus was placed on the region in the vicinity of the cutting edge at the rear of the bucket because this

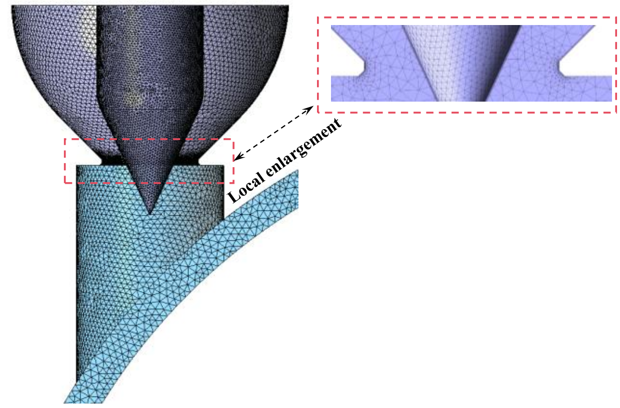

(a) Nozzle discretization

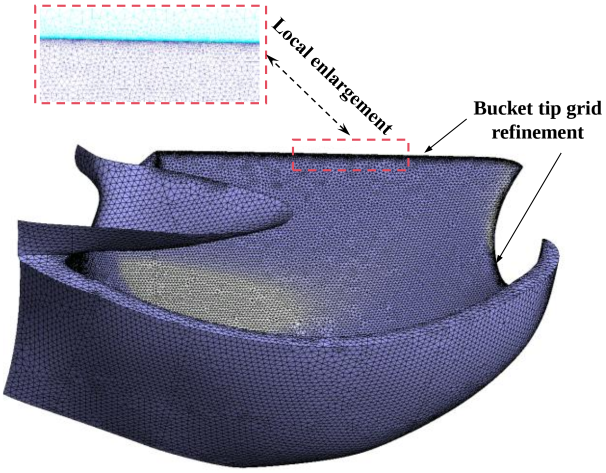

(b) Bucket discretization

Fig. 2 Mesh discretization results

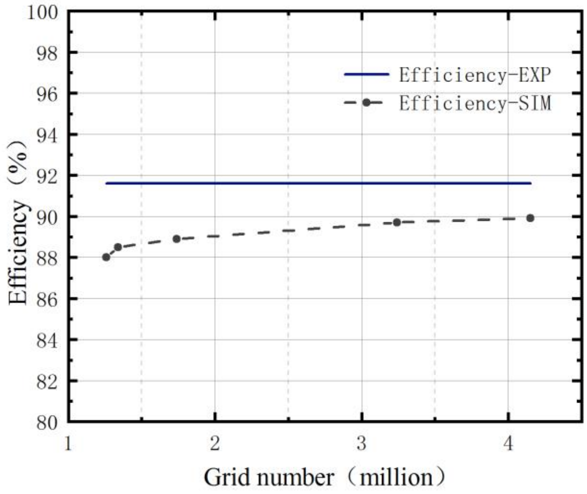

Fig. 3 Validation of the turbine hydraulic efficiency results generated with different mesh configurations

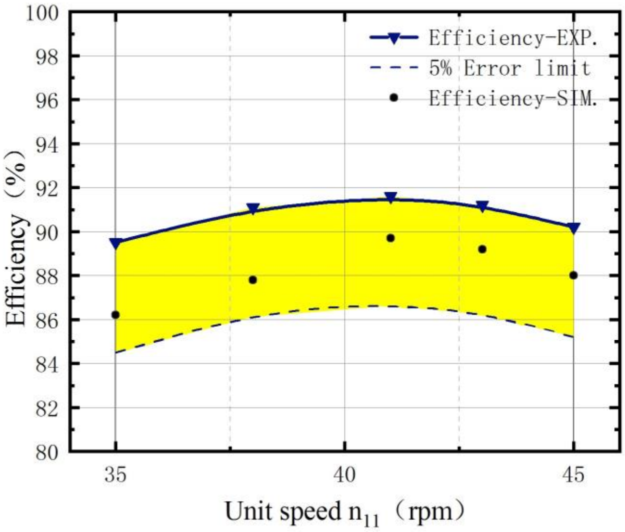

Fig. 4 Experimental and calculated hydraulic efficiency values obtained at various rotational speeds

area is susceptible to cavitation; thus, the mesh refinement was intensified in this region. Similarly, in the outlet contraction section of the nozzle and at the nozzle tip, targeted mesh refinement was performed to account for the effects of the viscous stresses exerted by the flow on the wall surfaces.

To assess the effects of mesh resolution on the simulation accuracy, a comprehensive analysis that utilized five distinct mesh configurations with varying node densities was performed for a single bucket. These configurations included 1.26, 1.34, 1.74, 3.24, and 4.05 million elements. As the element size decreased and the number of elements increased, the mesh density per unit area increased correspondingly, thereby facilitating a more nuanced depiction of the complex geometry of the bucket. For validation purposes, an optimal unit speed, n_{11}, of 41 r/min and an optimal needle stroke, Sn, of 24 mm were selected as benchmark values for the simulations conducted with the various mesh configurations. Figure 3 presents the results of the comparative analysis, where the blue line represents the experimentally determined rated efficiency, while the black points denote the calculated efficiency values for all the mesh configurations. The results indicate that the simulated turbine efficiency gradually rose under these optimal conditions as the number of mesh elements increased.

When grids with 1.26, 1.34, 1.74, 3.24, and 4.05 million elements were used for a single bucket, calculated efficiencies equal to 96.07, 96.62, 97.05, 97.87, and 98.14% of the experimental efficiency were obtained, respectively. It is worth noting that, when 3.24 million elements were used in the mesh of a single bucket, the computational values stabilized to a value approximately 2% below the experimental value. This stabilization suggests that, when a mesh with 3.24 million elements is utilized, a reliable simulation of the turbine performance under optimal conditions can be achieved.

To further validate the selected mesh configuration, simulations of the turbine were conducted for five different rotational speeds. Each employed a single-bucket mesh with 3.24 million elements. The results are presented in Fig. 4. Ratios of the numerical simulation efficiency to the model test efficiency of 96.31, 96.60, 97.87, 97.81, and 97.56% were obtained for rotational

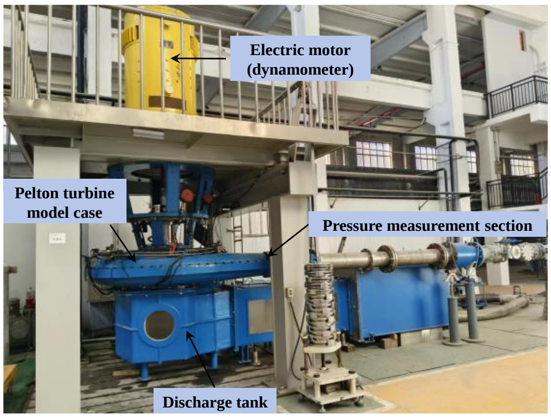

(a) Experimental setup

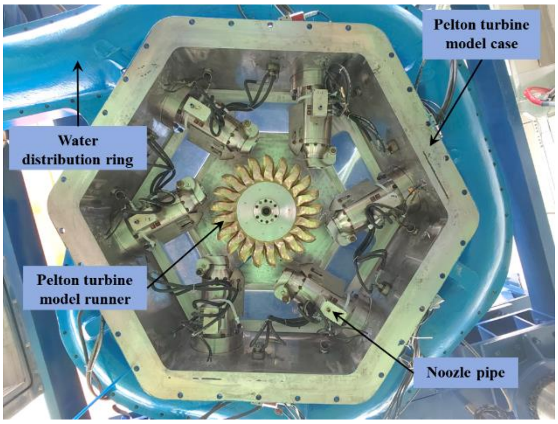

(b) Internal structure of the experimental device

Fig. 5 Pelton turbine testing system

speeds of 35, 38, 41, 43, and 45 r/min, respectively. This analysis indicates that the optimal rotational speed that maximizes the hydraulic efficiency is approximate. At the optimal point, the simulated single-nozzle flow rate was 28.87 L/s, while an experimental flow rate of 28.36 L/s was obtained during model testing.

Deviations from this optimal speed, regardless of the direction, led to decreases in hydraulic efficiency. Moreover, the calculated values demonstrated a consistent correlation with the experimental data; the discrepancies between the two sets of results remained relatively stable for all the tested rotational speeds. This consistency clearly shows that the selected mesh configuration can accurately predict the turbine performance across a variety of operating conditions.

3.3 Experimental Validation

The accuracy of the simulation calculations could be more reliably validated by comparing the calculations with the results of model experiments. Such a comparison would confirm the correctness of the mesh discretization scheme and the boundary condition settings. Therefore, model experiments were conducted with a Pelton turbine runner. The experimental setup, which is illustrated in Fig. 5, adhered to relevant IEC standards and primarily consisted of a model case, a distribution ring, a nozzle pipe, a discharge tank, and a runner.

This testing platform was specifically designed for high-parameter, high-precision experiments with hydraulic machinery related to Pelton turbines, and it fully complied with both international and national standards. The flow rate of the Pelton turbine was controlled by nozzle adjustments; the axial motion of the needle modulated the area of the nozzle throat, thereby enabling precise flow regulation. For these physical hydraulic tests, H62 copper was selected as the bucket material, while 06Cr19Ni10 stainless steel was used for the water distribution ring and the nozzle pipe. The platform had an overall measurement error of ≤ ±0.25%. A Rosemount 3051CD differential pressure sensor was used to measure the head, while the rotational speed was monitored with an MP-981 magnetic-induction speed sensor. The flow rate was measured with an ABB electromagnetic flowmeter (model DN200), and a GWT MP47/22C3 force sensor was utilized to measure the force. The torque on the runner was calculated as the product of the measured force and the length of the standard lever arm. Pressure measurement points, which were used to determine the model head, were situated at the inlet section of the distribution ring, and the static pressure was recorded using a Rosemount 3051CD differential pressure sensor. The static pressure measurements were then combined with the dynamic pressure measurements from the inlet pipe to obtain the turbine head. An uncertainty analysis was conducted for the Pelton turbine model tests to evaluate the reliability of the efficiency results. The standard uncertainties of the primary measured parameters were derived from their respective instrument accuracies. These sensor measurement accuracies include a flow rate accuracy of ±0.1%, a water head accuracy of ±0.1%, a torque accuracy of ±0.05%, and a rotational speed accuracy of ±0.06%. The combined standard uncertainty of the efficiency, η, was calculated using error propagation, which considered the partial derivatives of η with respect to each parameter. A combined standard uncertainty of 0.05 was obtained.

The nozzle configurations for the Pelton turbine experiments included one, two, three, four, and six nozzles. The specific rotational speed of the runner was adjusted by varying the dynamometer speed, while the specific flow rate of the turbine was regulated by changing the stroke of the nozzle pipe. The numerical calculation approach that was employed during this study effectively reflected the experimental conditions. The similarity conditions between the numerical calculations, model experiments, and prototype operation were established through unit similarity conversions. The expressions for the unit speed and the unit flow rate are provided in Eq. (6):

$$\begin{cases} n_{11} = \frac{n \times D_1}{\sqrt{H}} \\ Q_{11} = \frac{Q}{{B_2}^2\sqrt{H}} \end{cases} \tag{6}$$

where Q represents the flow rate, H denotes the experimental water head (60 m), D_1 is the diameter of the runner pitch circle (423.6 mm), and B_2 represents the width of the bucket interior (103.02 mm).

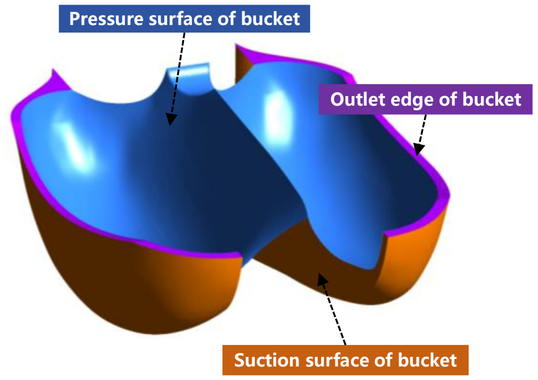

Fig. 6 Surface categorization for the Pelton turbine bucket

The experiments were conducted under a constant head. The unit speed was adjusted by varying the rotational speed of the electric motor, while the unit flow rate was regulated by changing the needle stroke. Taking a single-nozzle test as an example, the needle was opened with an initial stroke of 3 mm. The model inlet head was set to 60 m, and the motor speed was adjusted to achieve a unit speed of 35 r/min. The turbine efficiency and unit flow rate were both measured. Subsequently, the unit speed was increased in increments of 2 r/min until it reached 45 r/min. Then, the flow rate was increased by employing stroke increments of 3 mm. Finally, according to the unit flow rate and the unit speed, iso-efficiency curves were plotted to obtain an efficiency curve for the single-nozzle condition.

4. MECHANISMS OF THE SUCTION SURFACE OF THE PELTON TURBINE BUCKET

4.1 Analysis of Torque Characteristics of the Pelton Turbine Bucket

The Pelton turbine bucket is comprised of intricate curved surfaces. Therefore, a systematic examination of the contribution of the suction surface to the torque curve is necessary. The various surfaces of the bucket were meticulously categorized during this study, as Fig. 6 shows. The pressure surface, the suction surface, and the outlet edge were all identified. Throughout the rotational operation of the bucket, the positions of these surfaces relative to the jet continuously change. These changes lead to dynamic fluctuations in the torque on each surface, which in turn induce variations in the external characteristic torque and efficiency.

The resultant force that acts on the bucket is composed of three components: a force that acts on the pressure surface, a force that acts on the suction surface, and a force that acts on the outlet edge. This resultant force can be expressed by Eq. (7):

$$T_z = \iint_{A_p} \left(r_p \times [\tau_p] \cdot N_p\right) d_{A_p} + \iint_{A_s} \left(r_s \times [\tau_s] \cdot N_s\right) d_{A_s} + \iint_{A_o} \left(r_o \times [\tau_o] \cdot N_o\right) d_{A_o} \,, \tag{7}$$

where A represents the bucket area, subscripts p, s, and o denote the pressure surface, the suction surface, and the outlet edge, respectively, r is the radial vector, τ is the wall stress, N is the direction of the phase vector that is normal to the wall, and z represents the direction of the rotation axis. To facilitate an investigation of the influence of the suction surface on the torque curve of the bucket, a computational analysis coordinate system was established for the bucket, as shown in Fig. 7. Within this coordinate system, the jet was aligned such that its flow direction is vertically downward, while the buckets rotate in a counterclockwise direction. The angle θ was defined as the angular displacement between the positive Y-axis and the line that connects the vertex of the cutting edge of the bucket with the rotation center. In addition, the counterclockwise direction was considered to be the positive rotation direction.

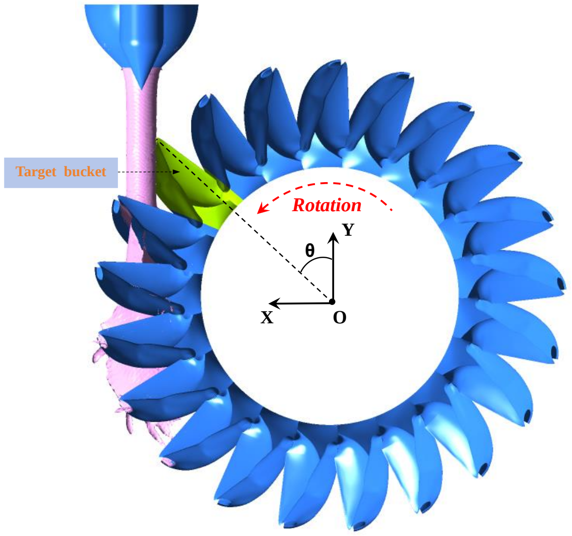

Fig. 7 Computational-analysis coordinate system for the bucket

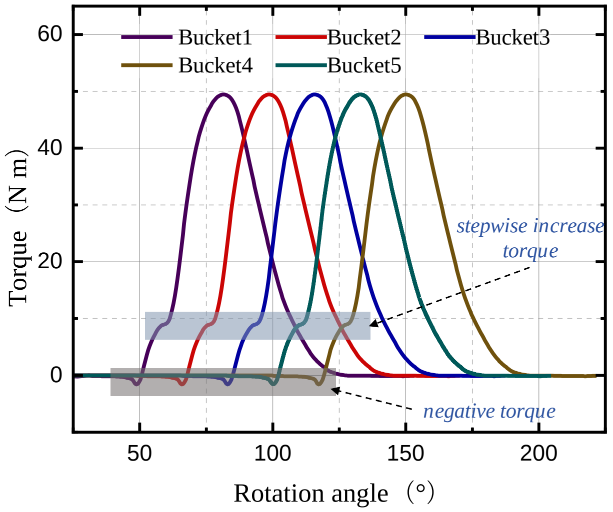

Fig. 8 Torque curves for five consecutive buckets

This portion of the investigation focused on a series of five buckets, and the torque fluctuations that are produced under the influence of a single jet were scrutinized. Figure 8 shows that the torque profiles for these buckets have similar contours but are phase-shifted with respect to each other; the torque graph for each bucket is delayed by (360/21)° from that for the preceding

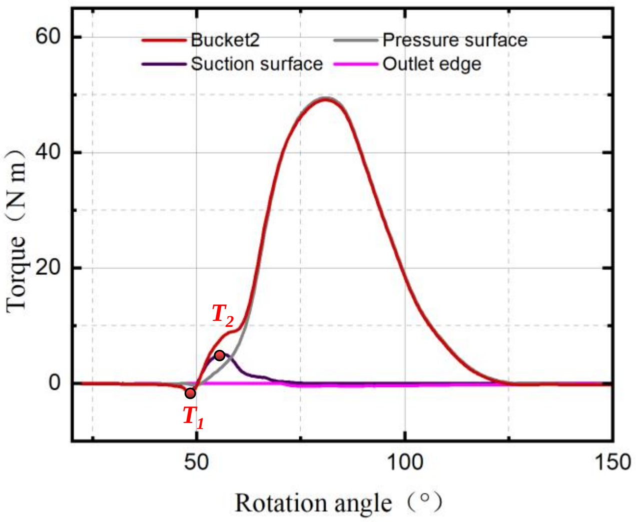

Fig. 9 Decomposition of the torque curve of the target bucket

bucket. These phase shifts are attributable to the uniform arrangement of 21 buckets around the circumference of the rotating runner. Observations of the buckets revealed that, at the onset of the jet impact, each bucket endures a transient period in which the torque is negative. After this initial phase, each torque graph exhibits a stepwise increase, after which the torque increases rapidly until it reaches a peak value. The torque subsequently declines until it ultimately approaches a near-zero asymptotic value.

4.2 Analysis of the Suction Surface of the Pelton Turbine Bucket

In an attempt to understand the nuances of the torque fluctuations within the buckets of Pelton turbines—and particularly the negative torque and stepwise torque increase phenomena—the focus was placed on Bucket 2 during this study. Its torque curve was meticulously scrutinized. The data presented in Fig. 9 reveal that the negative torque measurements are predominantly gathered from the suction surface of the bucket. This negative torque phenomenon occurs the instant that the bucket makes initial contact with the jet; at this time, the torque vector on the suction surface of the bucket is in the direction opposite to the rotation direction (Zhao et al., 2023b). Moreover, the stepwise increments in the torque curve are also associated with the suction surface, and they occur when the bucket is still in contact with the jet. At this point, the torque vector on the suction surface is in the rotation direction. Conversely, the pressure surface of the bucket sustains a positive torque throughout the entire jet flow cycle, which demonstrates a relatively stable variation pattern. Additionally, the torque at the outlet edge remains near zero throughout the flow cycle; therefore, it only minimally impacts the total torque. In summary, the suction surface exerts a substantial influence on the bucket torque during the dynamic bucket–jet interactions. These results emphasize the importance of making the bucket suction surface a focal point of further investigations regarding the operational mechanics of Pelton turbine buckets.

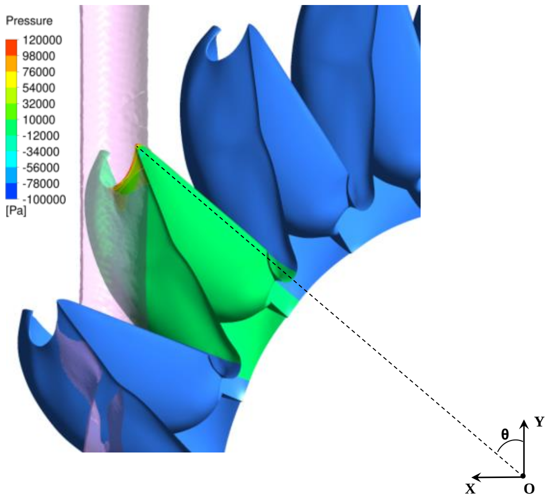

(a) Instant T1

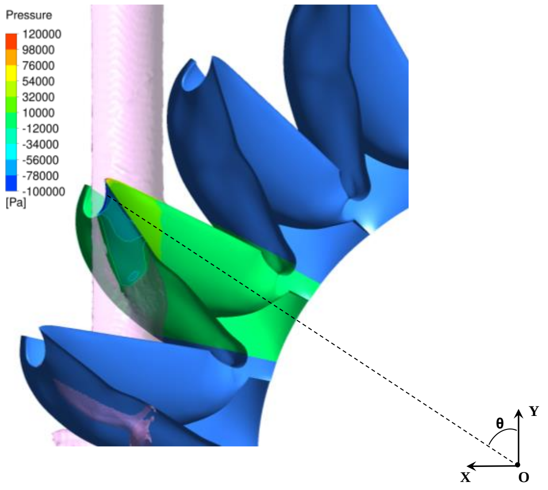

(b) Instant T2

Fig. 10 Relative positions of the target bucket at different instants.

The precise instant T1 marks the point at which the negative torque on the suction surface of the bucket peaks at a rotational angle of 48.7°. Figure 10(a) shows that, at this point, the entire cutting edge of the bucket is fully submerged within the jet. The results of CFD simulations reveal a high-pressure zone at the leading edge of the bucket suction surface; this high-pressure zone is perpendicular to the suction surface and is in the direction opposite to the rotation direction. This pressure distribution engenders a negative torque during the bucket revolution, thereby hindering the operational performance of the bucket. At this time, the resistance on the suction surface surpasses the driving force that acts on the pressure surface, which causes the entire bucket to exhibit a state of negative torque.

The precise instant T2 marks the point at which the positive torque on the suction surface of the bucket reaches its maximum value at a rotational angle of 57.2°. Figure 10(b) shows that, at this point, the entire cutting edge of the bucket has fully traversed the jet center. Numerical simulations corroborated the presence of a low-pressure region on the suction side, a phenomenon that was also observed during experimental studies conducted by EPFL (Perrig, 2007). This low-pressure zone generates a suction force on the suction surface that is oriented perpendicular to the suction surface and in the rotation direction. The distribution of this suction force facilitates increases in the bucket torque during the rotation process, thereby effectively augmenting the rotational momentum of the bucket.

Throughout the jet-impingement process, it was observed that the torque at the outlet edge of the bucket is effectively negligible because this region does not come into direct contact with the water flow. By the performance of an overlay analysis of the torque curves for the suction surface, the pressure surface, and the outlet edge of the bucket, an overall torque curve for the bucket was synthesized. This composite torque curve demonstrates that the bucket experiences an initial transient phase of negative torque during the jet-impingement process, after which it is subjected to a pronounced stepwise increase in positive torque.

5. ANALYSIS OF THE EFFECTS OF THE IMPINGEMENT ANGLE ON THE PERFORMANCE OF THE BUCKET

5.1 Quantitative Analysis of the Impingement Angle

Section 4 discusses the results of an in-depth analysis of the dynamics by which the suction surface of the bucket affects the jet-impingement process. To expand upon this understanding, the principal objective of this section is to explore the use of modifications to the suction surface design to optimize the runner torque output. Because of the dynamic nature of the interactions between the bucket and the jet, the impingement process is inherently subject to variations, and the impingement state is progressively transformed with time. Figure 11 shows that the jet issues from the nozzle at a high velocity while maintaining a cylindrical form. The cutting edge of the bucket is characterized as a space curve, which is a geometric attribute that implies non-simultaneous contact between various points along the cutting edge and the jet during the dynamic impingement process. Consequently, it was deduced that the angles at which the cutting edge contacts the jet will be different at different points along the edge.

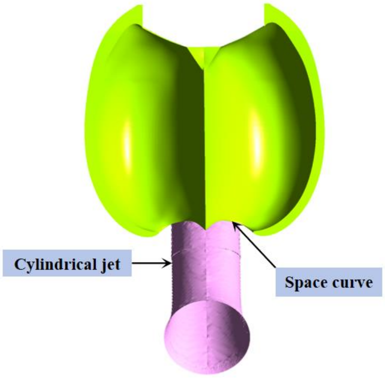

Fig. 11 Schematic representation of the relative positions of the jet and the bucket

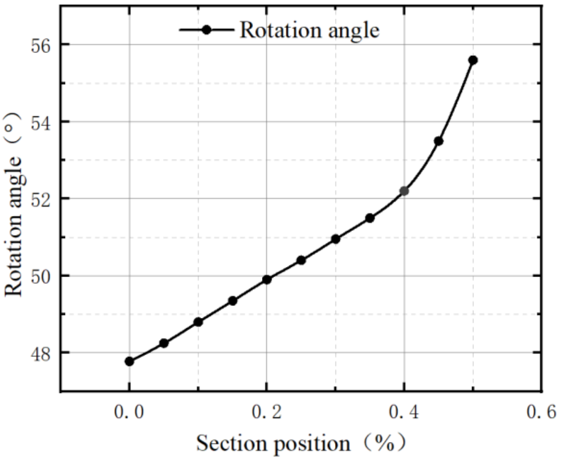

Fig. 12 Rotation angles of various points on the bucket cutting edge at the instant of initial jet contact

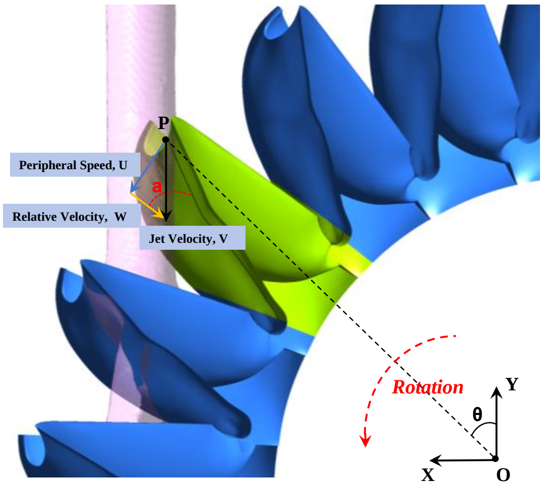

Fig. 13 Analysis of the initial jet impingement angle at point P along the bucket edge

To quantitatively characterize the interactions between the cutting edge of the bucket and the jet, the data were normalized with respect to the jet diameter during this study. By leveraging the cylindrical symmetry of the jet and the bucket symmetry, the detailed analysis could be focused on one half of the bucket. Half of the jet diameter was assigned a reference value of 0.5, and the rotational angles at which different points along the cutting edge of the bucket come into contact with the jet were determined. As is demonstrated by the data presented in Fig. 12, the vertex of the cutting edge contacts the jet first. As the bucket rotates, other points along the cutting edge engage with the jet. The outermost point is the last point to make contact. This sequential interaction process reveals the dynamic nature of the interactions between the bucket and the jet; thus, these results offer significant insights into the internal flow dynamics of the bucket.

To further explore the jet state at various points along the bucket cutting edge, a random point, P, on the cutting edge was selected for detailed examination. In Fig. 13, when P begins to interact with the jet, the corresponding cross-section is denoted by z and the rotational

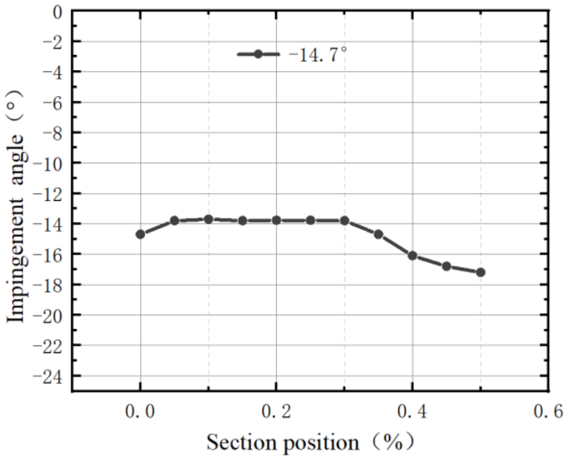

Fig. 14 Initial jet impingement angles at various locations on the bucket cutting edge

angle of the bucket is represented by θ. The jet velocity can be expressed by Eq. (8):

$$V = C_v\sqrt{2gH} \tag{8}$$

where C_v is the jet velocity coefficient, g represents the gravitational acceleration, and H is the hydraulic head of the turbine.

The relationship between the circumferential velocity, w, of the runner and its rotational speed, n, can be expressed by Eq. (9):

$$w = 2\pi n/60 \tag{9}$$

The coordinates of P are denoted as (x, y). From these, we can determine its rotational radius, $r = \sqrt{x^2 + y^2}$, and consequently, its peripheral speed, $U = wr$. By employing a fluid-dynamics vector analysis, the velocity, W, of the jet relative to the bucket was calculated for that instant. The angle between the relative velocity vector and the line of intersection with the suction surface is denoted as a; this angle is a critical parameter that reflects the flow state of the jet relative to the suction surface of the bucket.

A quantitative analysis of the impingement angles at various points along the cutting edge of the bucket was conducted using the method described above. Figure 14 demonstrates that not only are the rotation angles at initial jet–bucket contact different for the various points on the cutting edge, but the impingement angles also vary. The relative velocities directed toward the suction surface were defined as negative; therefore, the average impingement angle was found to be -14.7°. The relative motion between the jet and the suction surface is complex and variable. Specifically, the magnitude of the impingement angle is directly related to the intensity and direction of the jet flow when it impacts the suction surface of the bucket, and the angle magnitude in turn affects the torque contribution to the turbine shaft.

5.2 Analysis of the Impingement Angle Effects

To expand upon the analysis presented above, a simplified vector diagram that elucidates the initial jet dynamics at the cutting edge of the bucket was generated. This diagram facilitates a more transparent comprehension of the effects of the jet on the suction surface. The impingement angle of the jet as it impacts the bucket can be manipulated by altering the angle of the suction surface. Figure 15 demonstrates that reducing the thickness of the suction surface decreases the jet impingement angle, thus decreasing the detrimental effects of the jet on the suction surface. However, increasing the thickness of the suction surface produces a larger impingement angle, which amplifies the force exerted by the jet on the suction surface.

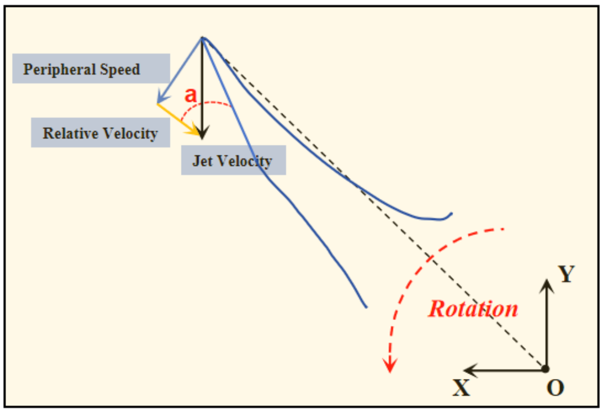

(a) Impingement angle illustration

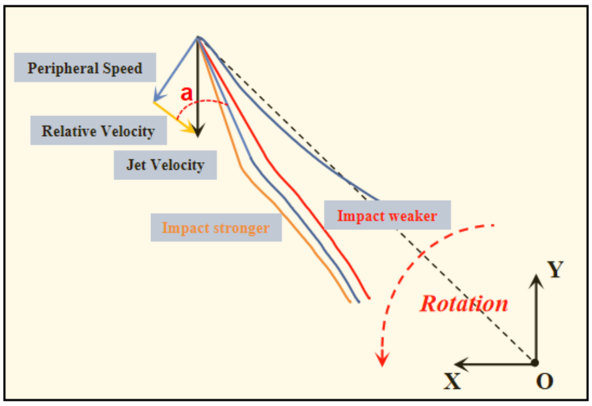

(b) Effects of impingement angle adjustments

Fig. 15 Schematic diagrams of the bucket impingement angle and its effects

To attain a more thorough understanding of how the impingement angle affects the interactions between the bucket and the jet, the flow characteristics at various impingement angles were studied by manipulating the thickness of the suction surface of the bucket.

The position of the vertex of the bucket cutting edge was held constant to ensure that the rotation angle at initial jet contact remained consistent. Then the thickness of the suction surface was adjusted to create three distinct design configurations: the original design, which has an average impingement angle of -14.7°, and designs with average impingement angles of -12.9° and -17.3°. The specific impingement angle variations for each of these configurations are depicted in Fig. 16.

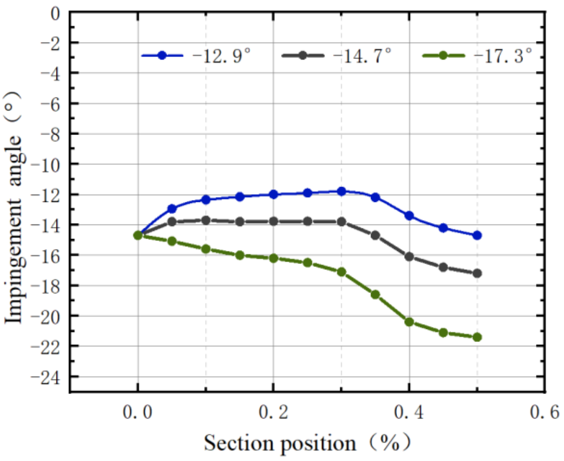

Fig. 16 Initial jet impingement angles for various design configurations

5.3 Adjusted Results of the Impingement Angle Effects

During this investigation, the torque responses for various bucket designs were analyzed under uniform operating parameters. Figure 17 presents the torque profiles for the suction surfaces of these designs. A comparative examination indicated that the impingement angle is crucial to the determination of the torque exerted on the suction surface of the bucket. Intriguingly, an increase in the impingement angle leads to increases in the magnitudes of both the positive and negative torques generated by the suction surface. Conversely, a reduction in the impingement angle produces decreases in the magnitudes of both the positive and negative torques. This observation emphasizes the significance of the impingement angle as a determinant of the torque output. Importantly, the impingement angle effects are manifested in amplitude modulation of the torque curve rather than in rotation angle shifts, which suggests that its effects are independent of the rotational position of the bucket.

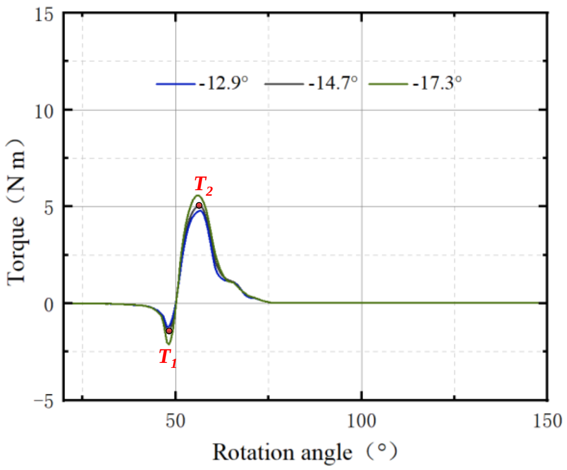

Fig. 17 Torque on the suction surface for various impingement angles

For the precise instant T_1, which corresponds to a bucket angle of 48.7°, a comparative analysis of the various design configurations was conducted. The results are depicted in Fig. 18, and they reveal that a decrease in the impingement angle leads to a contraction of the high-pressure zone on the suction surface, while an increase in the impingement angle results in an expansion of the high-pressure region along the cutting edge of the suction surface. These pressure fluctuations are indicative of the fundamental physical mechanisms that drive the torque variations. A smaller impingement angle mitigates the jet impact on the suction surface and thus leads to a decrease in the negative torque. However, a larger impingement angle intensifies the jet influence, which leads to an increase in the negative torque.

A comparative analysis of the various design configurations was also conducted for the precise instant T_2, which corresponds to a bucket angle of 57.2°. The results of this analysis are depicted in Fig. 19, indicating that a reduction in the impingement angle is associated with a decrease in the size of the low-pressure zone on the suction surface, while an increase in the impingement angle is correlated with an expansion of this low-pressure domain. The extent of the low-pressure region is intricately linked to the magnitude of the suction force that is imposed on the suction surface of the bucket. Notably, a larger low-pressure region leads to a greater suction force, which in turn increases the positive torque of the bucket.

The spatial distribution on the suction surface of the bucket was investigated at T_2 for various impingement angles when the pressure was no greater than -12,000 Pa. The results of this investigation are presented in Fig. 20. Setting the water volume fractions in these regions to 0.5 enabled the areas of these regions, the forces exerted upon them, and the resultant torques, to be determined. A comparative analysis of the results obtained for various impingement angles revealed that these variables are linearly correlated. By performing mathematical modeling, multiple relationships were established. The relationship between the area of the suction surface and the impingement angle (for a pressure of $\leq$ -12,000 Pa) was determined to be $y_1 = 0.0931\alpha + 6.3084$, and the fitting error, R^2, is 0.923. The relationship between the force on this region and the impingement angle can be expressed by $y_2 = 0.7160\alpha + 10.9247$, which has a fitting error of 0.992. Finally, the correlation between the torque generated by this force and the impingement angle can be represented by $y_3 = 0.1378\alpha + 2.5718$, which has a fitting error of 0.997. These fitting errors emphasize the robust correlation that exists between the empirical data and the model used during this study. Furthermore, an increase in the impingement angle is associated with consistently increasing trends in all the variables (area, force, and torque). This insight suggests that it is feasible to effectively modulate the torque during the jet-impingement process by precisely adjusting the impingement angle on the suction surface of the bucket. This conclusion has significant practical implications for Pelton-turbine efficiency optimization.

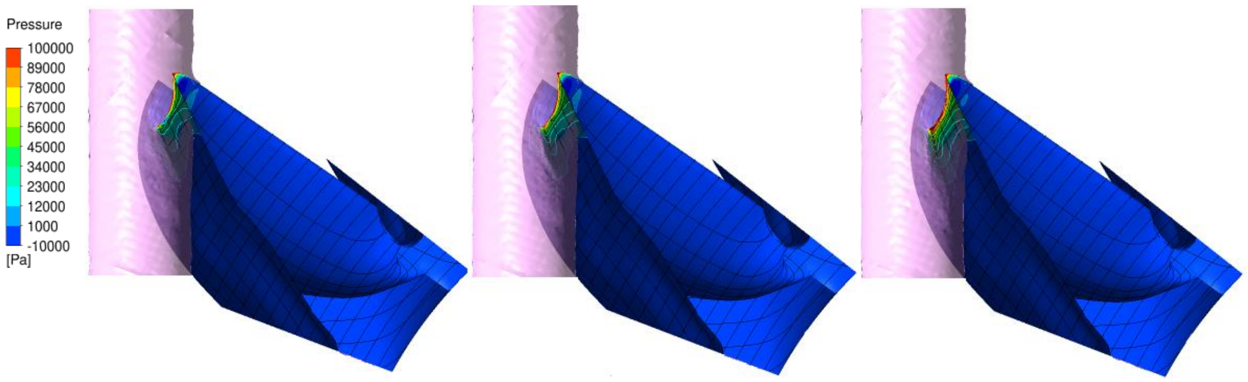

(a) $a = -12.9°$ (b) $a = -14.7°$ (c) $a = -17.3°$

Fig. 18 Relative positions of the target bucket at T$_1$ for various impingement angles

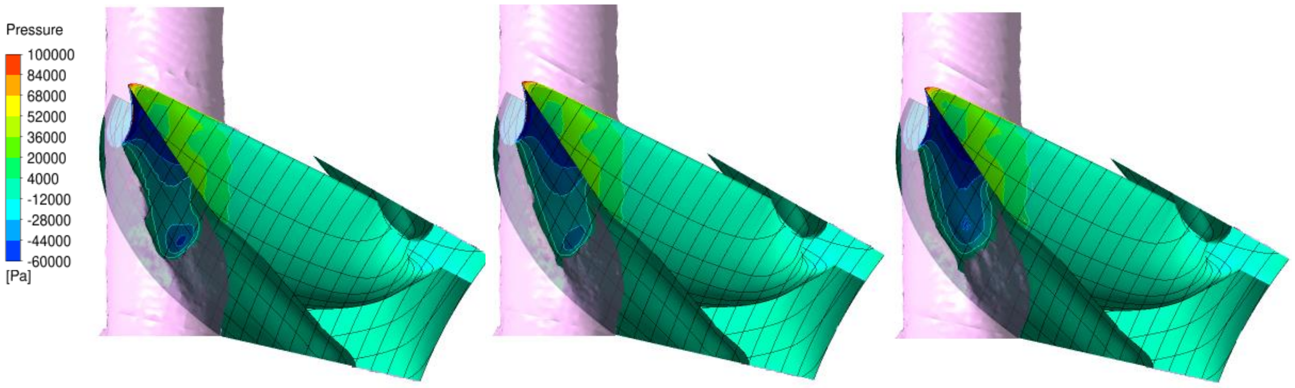

(a) $a = -12.9°$ (b) $a = -14.7°$ (c) $a = -17.3°$

Fig. 19 Relative positions of the target bucket at T$_2$ for various impingement angles

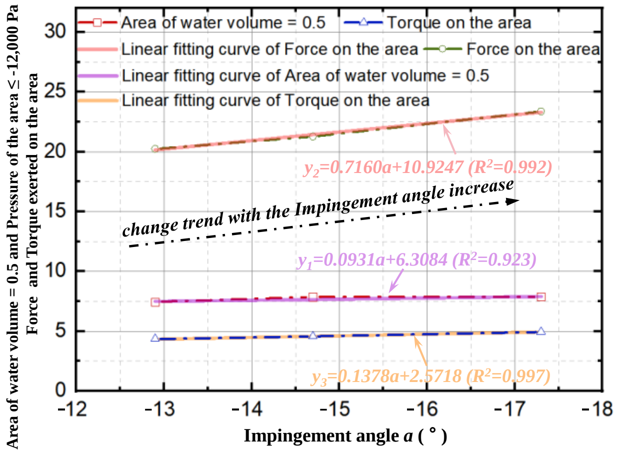

Fig. 20 Area ratios of the key variable relationships at various impingement angles

A meticulous examination of the combined torque curve for the target bucket revealed a distinct stepwise augmentation in the torque; this augmentation is predominantly driven by the positive torque that is exerted on the suction surface. This pattern was observed to be consistent across a variety of scenarios as the torque increases to its maximum value. However, as the torque begins to decrease, disparities between the torque curves for various configurations become apparent. Figure 21 illustrates that the configuration with an average impingement angle of -17.3° has a smaller combined torque than the other configurations. Conversely, the configuration with an average impingement angle of -12.9° has the largest combined torque. These findings demonstrate the substantial effects that variations in the impingement angle exert on the combined torque of the bucket as it decreases from its maximum value.

At the precise instant T$_3$, which corresponds to a bucket rotation angle of 90.2°, the target bucket experiences the impact of a jet flow that has been redirected by the preceding bucket. With respect to the baseline scenario, for which the impingement angle is -14.7°, the torque for the configuration with an impingement angle of -12.9° increases by 1.18%, while the torque for the configuration with an impingement angle of -17.3° decreases by 2.04%. Figure 22 illustrates the flow patterns at the split-edge plane; in the figure, the vertical yellow line serves as a reference and the red line indicates the contour for which the water volume fraction is equal to 0.5. This analysis revealed that the right boundary of the jet flow in the -14.7° scenario closely aligns with that in the baseline scenario, while the right boundary in the -12.9° scenario surpasses it. In contrast, the right boundary in the -17.3° scenario does not reach the boundary in the baseline scenario.

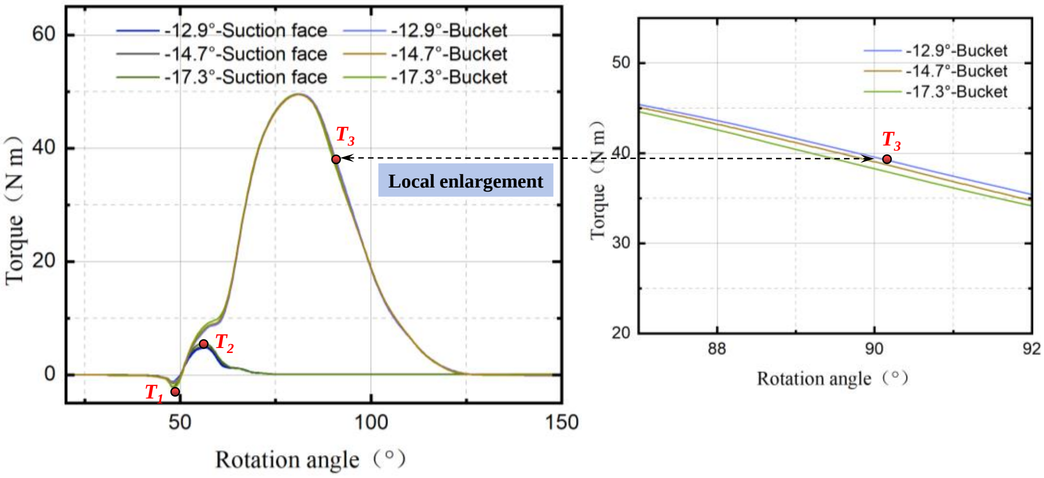

Fig. 21 Combined torque curves of the target bucket for various impingement angles

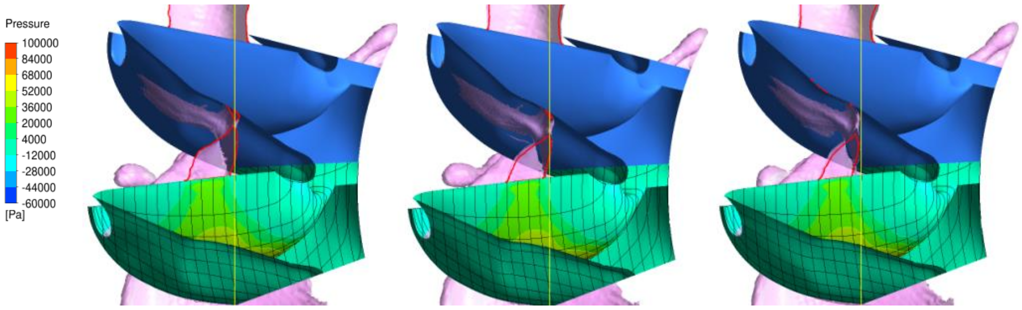

(a) $a = -12.9°$ (b) $a = -14.7°$ (c) $a = -17.3°$

Fig. 22 Relative positions of the target bucket at T$_3$ for various impingement angles

These findings indicate that impingement-angle variations significantly affect the incidence location of the jet flow on the subsequent bucket. An increase in the impingement angle intensifies the low-pressure region on the suction surface, thereby amplifying the pulling effect on the jet and impeding its motion toward the base of the bucket. This shift influences the position at which the jet strikes the bucket, thus impacting the torque and efficiency of the bucket. Therefore, methods of adjusting the impingement angle are pivotal to the early stages of the jet-impingement process and they significantly influence the performance of the subsequent bucket. When designing and optimizing Pelton buckets, it is imperative to consider the effects of the impingement angle on both the suction and pressure surfaces, as well as how these factors interact to enhance the overall performance of the bucket.

6. CONCLUSIONS

This work provides a comprehensive analysis of the effects of the suction surface of a Pelton turbine bucket and the jet-impingement angle on the overall bucket performance. The following primary conclusions were obtained.

(1) A systematic analysis of the pressure and torque on Pelton bucket surfaces revealed the dynamic torque generation mechanism. During initial jet engagement ($\theta = 48.7°$), a high-pressure zone develops at the leading edge of the suction surface and generates a transient negative torque. As rotation progresses ($\theta = 57.2°$), the state of the suction surface transitions such that a negative-pressure region is formed; this negative pressure promotes rotation, which leads to a step-like increase in the torque. This pressure-transition process explains why the dynamic torque shifts from negative values to abrupt increases.

(2) The impingement angle, which is defined as the included angle between the relative velocity of the jet and the suction-surface intersection line, was found to be a key control parameter. A quantitative analysis demonstrated that significant impingement-angle variations (that range from -17.3 to -12.9°) occur along the cutting edge of the bucket. Thus, it confirmed that the impingement angle can effectively characterize the flow interference intensity at the interface between the jet and the suction surface.

(3) Precisely controlling the thickness of the bucket suction surface, and thereby adjusting the impingement angle, can significantly enhance the jet–bucket interaction characteristics. A reduction in the impingement angle causes the low-pressure zone on the suction surface to expand. This expansion enhances the jet adsorption effect and effectively prevents jet deviation toward the bucket base. This adjustment simultaneously alters the trajectory of the detached jet, which affects the

jet impact position on the subsequent bucket. At a rotation angle of 90.2°, the torque increases by 1.18% and decreases by 2.04% for configurations with impingement angles of -12.9 and -17.3°, respectively, with respect to the baseline scenario (which has an impingement angle of -14.7°). These findings provide critical insights into the use of impingement-angle adjustments as a means of optimizing the overall turbine performance.

Although significant results were achieved during the present investigation, they were accompanied by certain constraints. Subsequent studies should focus on refining the geometric design of the bucket cutting edge to optimize the impingement-angle distribution at multiple locations. This optimization could lead to increases in the energy-conversion efficiency and the reliability of the power output. Additionally, the simulations performed during this study only utilized a single-nozzle configuration, which may restrict the broader applicability of the results. In scenarios that involve multiple nozzles, the complexity of the flow interactions in Pelton turbines increases significantly. Therefore, addressing this complexity is a vital direction for future research in the field of flow-dynamics simulations of Pelton turbines.

ACKNOWLEDGMENTS

This document is the result of a research project funded by the National Key R&D Program of China (No. SQ2023YFB3408401) and the Natural Science Foundation of China (Grant No. 52476026). We thank LetPub (www.letpub.com.cn) for its linguistic assistance during the preparation of this manuscript.

CONFLICT OF INTEREST

The authors declare no conflict of interest.

AUTHOR CONTRIBUTIONS

Yongxin Liu: Conceptualization, Methodology, Software, Validation, Formal Analysis, Investigation, Data Curation, Writing of the Original Draft, Writing of the Final Manuscript, Review, Editing, and Visualization. **Qun Zheng:** Methodology, Validation, and Review. **Lianheng Guo:** Supervision, Methodology, Review, and Editing. **Xianzhu Wei:** Methodology, Validation, and Review. **Bin Xu:** Data Curation and Validation. **Huanmao Wang:** Formal Analysis and Investigation. **Daqing Qin:** Methodology, Validation, and Review. **Lei Han:** Software, Validation, and Editing.

REFERENCES

Chitrakar, S., Solemslie, B. W., Neopane, H. P., & Dahlhaug, O. G. (2020, Oct). Review on numerical techniques applied in impulse hydro turbines [Review]. *Renewable Energy*, *159*, 843-859. https://doi.org/10.1016/j.renene.2020.06.058

CREEI (2023). China's Renewable Energy Development Report. https://www.in-en.com/article/html/energy-2333306.shtml.

Erazo, J., Barragan, G., Pérez-Sánchez, M., Tapia, C., Calahorrano, M., & Hidalgo, V. (2022). Geometrical optimization of pelton turbine buckets for enhancing overall efficiency by using a parametric model-a case study: Hydroelectric power plant "Illuchi N2" from Ecuador. *Energies*, *15*(23), 9052. https://doi.org/10.3390/en15239052

Fan, W. R., Sun, L. G., & Guo, P. C. (2024. Investigation on unstable flow characteristics and energy dissipation in Pelton turbine. *Engineering Applications of Computational Fluid Mechanics*, *18*(1), 2304643. https://doi.org/10.1080/19942060.2024.2304643

Han, L., Guo, C., Osman, F. K., Li, D., Wang, H., Liu, Y., & Qin, D. (2024). Effect and mechanism of erosion in Pelton turbine and case studies-A review [Review]. *Physics of Fluids*, *36*(3), 031301. https://doi.org/10.1063/5.0191051

Han, L., Wang, Y., Zhang, G. F. & Wei, X. Z. (2021). Investigation of the erosion characteristics in the distribution parts of pelton turbine. *Journal of Applied Fluid Mechanics*, *14*(6), 1809-1816. https://doi.org/10.47176/jafm.14.06.32868

IHA (2022). Hydropower status report. https://www.hydropower.org/publications/2022-hydropower-status-report.

Janetzky, B., Göde, E., Ruprecht A., Keck H., & Schärer C. (1998). *Numerical simulation of the flow in a Pelton bucket.* Proceedings of the 19th IAHR Symposium on Hydraulic Machinery and Cavitation. https://jglobal.jst.go.jp/en/detail?JGLOBAL_ID=200902138953689530

Jošt, D., Mežnar, P., & Lipej, A. (2010). *Numerical prediction of Pelton turbine efficiency*. The 25th IAHR Symposium on Hydraulic Machinery and Systems. https://www.semanticscholar.org/paper/Numerical-prediction-of-Pelton-turbine-efficiency-Jo%C5%A1t-Mez%CC%8Cnar/2b2e67ba7cd0fac0f5edfe48b6adf5f86a882baf

Menter, F. R. (1994). Two-equation eddy-viscosity turbulence models for engineering applications. *AIAA Journal*, *32*, 1598-1605. https://www.semanticscholar.org/paper/Two-equation-eddy-viscosity-turbulence-models-for-Menter/7f0a37725a836b3460a4e1a67a2b66dc69800a36

Messa, G. V., Mandelli, S., & Malavasi, S. (2019, Jan). Hydro-abrasive erosion in Pelton turbine injectors: A numerical study. *Renewable Energy*, *130*, 474-488. https://doi.org/10.1016/j.renene.2018.06.064

Mirza Umar, B., Wang, Z., Chitrakar, S., Thapa, B., Huang, X., Poudel, R., & Karna, A. (2024). Experimental erosion flow pattern study of pelton runner buckets using a non-recirculating test rig. *Energies*, *17*(16), 4006. https://doi.org/10.3390/en17164006

Nedelcu, D., Cojocaru, V., & Avasiloaie, R. C. (2021, Aug). Numerical investigation of nozzle jet flow in a pelton microturbine [Article]. *Machines*, *9*(8), 158. https://doi.org/10.3390/machines9080158

Padhy, M., & Saini, R. (2009). Effect of size and concentration of silt particles on erosion of Pelton turbine buckets. *Energy*, *34*(9), 1477–1483. https://doi.org/10.1016/j.energy.2009.03.027

Perrig, A. (2007). *Hydrodynamics of the free surface flow in Pelton turbine buckets* [PhD Thesis]. Swiss Federal Institute of Technology Lausanne (EPFL), Lausanne, Switzerland. https://infoscience.epfl.ch/record/109998

Perrig, A., Avellan, F., Kueny, J. L., Parkinson, E., & Farhat, M. (2006). Flow in a Pelton turbine bucket: Numerical and experimental investigations. *Journal of Fluids Engineering*, *128*(3), 350-358. https://doi.org/10.1115/1.2170120

PRC. (2021, March 13th). The 14th Five-Year Plan (2021-2025) for National Economic and Social Development and Vision 2035 of the People's Republic of China. https://www.gov.cn/xinwen/2021-03/13/content_5592681.htm

Shahram, D., Mohammad, B. M., & Ehsan, A. (2014). Numerical and experimental study of the effects of physical and the geometrical parameters on efficiency of a micro-Pelton turbine. *Journal of Renewable and Sustainable Energy Reviews*, *40*, 557-563. https://doi.org/10.1016/j.rser.2014.07.185

Smirnov, P. E., & Menter, F. R. (2009). Sensitization of the SST turbulence model to rotation and curvature by applying the spalart-shur correction term. *Journal of Turbomachinery-Transactions of the Asme*, *131*(4), 041010. https://doi.org/10.1115/1.3070573

Smirnov, P. E., Menter, F. R., & Asme. (2008, Jun 09-13). *Sensitization of the SST turbulence model to rotation and curvature by applying the spalart-shur correction term.* 53rd ASME Turbo Expo 2008, Berlin, Germany. https://asmedigitalcollection.asme.org/GT/proceedings-abstract/GT2008/43161/2305/334484

Solemslie, B. W., & Dahlhaug, O. G. (2012, Aug 19-23). *A reference Pelton turbine design. IOP Conference Series-Earth and Environmental Science.* 26th IAHR Symposium on Hydraulic Machinery and Systems, Tsinghua Univ, Beijing, PEOPLES R CHINA. https://iopscience.iop.org/article/10.1088/1755-1315/15/3/032005

Suyesh, B., Parag, V., Keshav, D., Ahmed, A., & Abdul-Ghani, O. (2019). Novel trends in modelling techniques of Pelton Turbine bucket for increased renewable energy production. *Renewable & Sustainable Energy Reviews*, *112*, 87-101. https://doi.org/10.1016/j.rser.2019.05.045

Viollet, P. L. (2017, 07/01). From the water wheel to turbines and hydroelectricity. Technological evolution and revolutions. *Comptes Rendus Mécanique*, *345*. https://doi.org/10.1016/j.crme.2017.05.016

Xiao, Y. X., Han, F. Q., Zhou, J. L., & Kubota, T. (2007, Jun). Numerical prediction of dynamic performance of Pelton turbine. *Journal of Hydrodynamics*, *19*(3), 356-364. https://doi.org/10.1016/s1001-6058(07)60070-5

Zeng, C. (2018). *Research on the internal flow characteristic and flow interference in the Pelton turbine*. [Doctoral dissertation, Tsinghua University]. https://link.cnki.net/doi/10.27266/d.cnki.gqhau.2018.000361

Zeng, C. J., Xiao, Y. X., Xu, W., Wu, T., Zhang, J., Wang, Z. W., Luo, Y. Y., & Iop. (2016, Jul 04-08). *Numerical analysis of pelton nozzle jet flow behavior considering elbow pipe. iop conference series-earth and environmental science.* 28th IAHR Symposium on Hydraulic Machinery and Systems (IAHR), Grenoble, FRANCE. https://iopscience.iop.org/article/10.1088/1755-1315/49/2/022005

Zhang, Z. (2017). Development and New Technology of Pelton Turbines, *Large Electric Machine and Hydraulic Turbine* (4), 1-6. https://doi:10.3969/j.issn.1000-3983.2017.04.001

Zhao, H. R., Xu, B., Tang, P., Guo, N., & Zhu, B. S. (2023a). Generation mechanism and control method of countertorque in the bucket of a Pelton turbine. *Physics of Fluids*, *35*(10), 105133. https://doi.org/10.1063/5.0174186

Zhao, H., Zhu, B., Xu, B., Tang, P., Guo, N., & Zhang, W. (2023b). Investigation on the influence of bucket's flow patterns on energy conversion characteristics of Pelton turbine. *Engineering Applications of Computational Fluid Mechanics*, *17*(1), 1-25. https://doi.org/10.1080/19942060.2023.2234435

Zhao, H., Zhu, B., & Jiang, B. (2025). Comprehensive assessment and analysis of cavitation scale effects on energy conversion and stability in pumped hydro energy storage units. *Energy Conversion and Management*, *325*, 119370. https://doi.org/10.1016/j.enconman.2024.119370

Zidonis, A., & Aggidis, G. A. (2015). State of the art in numerical modelling of Pelton turbines. *Renewable & Sustainable Energy Reviews*, *45*, 135-144. https://doi.org/10.1016/j.rser.2015.01.037

Zoppé, B., Pellone, C., Maitre, T., & Leroy, P. (2006). Flow analysis inside a Pelton turbine bucket. *Journal of Turbomachinery-Transactions of the Asme*, *128*(3), 500-511. https://doi.org/10.1115/1.2184350